Nanoscale

The role of ligands in electron transport in nanocrystal solids

Journal:	*Nanoscale*
Manuscript ID	NR-ART-09-2020-006892.R1
Article Type:	Paper
Date Submitted by the Author:	29-Oct-2020
Complete List of Authors:	Khabibullin, Artem; US Naval Research Laboratory, Center for Materials Physics and Technology Efros, Alexander; US Naval Research Laboratory, Canter for computational Material Scienec Erwin, Steven; US Naval Research Laboratory, Center for Materials Physics and Technology

Journal Name

ARTICLE TYPE

Cite this: DOI: 00.0000/xxxxxxxxxx

The role of ligands in electron transport in nanocrystal solids†

Artem R. Khabibullin,[a] Alexander L. Efros,[b] and Steven C. Erwin*[b]

Received Date
Accepted Date

DOI: 00.0000/xxxxxxxxxx

We investigate theoretically the transport of electrons and holes in crystalline solids consisting of three-dimensional arrays of semiconductor nanocrystals passivated by two types of organic ligands—linear chain carboxylates and functionalized aromatic cinnamates. We focus on a critical quantity in transport: the quantum-mechanical overlap of the strongly confined electron and hole wavefunctions on neighboring nanocrystals. Using results from density-functional-theory (DFT) calculations, we construct a one-dimensional model system whose analytic wavefunctions reproduce the full DFT numerical overlap values. By investigating the analytic behavior of this model, we reveal several important features of electron transport. The most significant is that the wavefunction overlap decays exponentially with ligand length, with a characteristic decay length that depends primarily on properties of the ligand and is almost independent of the size and type of nanocrystal. Functionalization of the ligands can also affect the overlap by changing the height of the tunneling barrier. The physically transparent analytic expressions we obtain for the wavefunction overlap and its decay length should be useful for future efforts to control transport in nanocrystal solids.

Nanocrystals are a distinct class of artificial materials whose electronic, magnetic, and optical properties are strongly controlled by size and shape. They can be also used as building blocks to create self-assembled nanocrystal solids having nearly crystalline order on a scale that would normally require lithography. The first nanocrystal solid was an "elemental" solid of CdSe nanocrystals grown by Murray and coworkers in 1995[1]. This work opened the door to more complex artificial electronic materials, and even to flexible electronics and nanocrystal-based integrated circuits, with widely tunable properties[2–4]. Good electron transport is a key requirement for these applications. Indeed, efforts to improve transport have increased the mobility of electrons in nanocrystal solids by more than five orders of magnitude since their discovery[5]. But further advances may require a more fundamental theoretical understanding of electron transport in these complex materials.

Electron transport in nanocrystal solids is, like the materials themselves, a complicated subject with many aspects requiring consideration[6–8]. There is a rich body of experimental data available for use as benchmarks against which theories can be tested. A much smaller number of theoretical works exist. One reason for this is that traditional analytic theories omit details of chemistry and geometry that are, in this case, often quite important[9]. At the same time, first-principles theoretical treatments that properly include these details do not readily allow one to draw more general conclusions. Nor do they always lead to clear principles that one can use for the rational design of better materials.

In this work we draw upon both approaches—first-principles and analytic—to formulate simple principles of conduction in nanocrystal solids that are by construction fully consistent with detailed atomistic calculations. We limit our scope to elemental nanocrystal solids: Bravais lattices with identical nanocrystals passivated by organic ligands, as shown schematically in Fig. 1(a). Such idealized structures might seem unrealistic, but recent multilayer diffraction experiments have indeed demonstrated that nanocrystal solids can approach the structural perfection of single crystals[10]. We exclude from our treatment several phenomena known to be important for conduction: carrier localization due to energy differences arising from nanocrystal size inhomogeneity[9,11], carrier trapping and recombination[8,12], excited-state quantum dynamics[13], polaron formation and reor-

[a] *NRC Research Associate, Resident at Center for Computational Materials Science, Naval Research Laboratory, Washington DC*
[b] *Center for Computational Materials Science, Naval Research Laboratory, Washington, DC; E-mail: steve.erwin@nrl.navy.mil*

† Electronic Supplementary Information (ESI) available: Computational methods for DFT calculations, DFT results for conduction wavefunctions, transfer-matrix solution of stepped square-well model, linearization of square-well equation and analytic expression for overlap integral and decay length, geometrical analysis of the effect of finite nanocrystal size on wavefunction overlap. See DOI: 00.0000/00000000.

S.C.E. and A.L.E. conceived the idea and supervised the project. S.C.E. and A.R.K. performed the DFT calculations. All authors contributed to the analytic theory. S.C.E. wrote the manuscript with input from the other authors.

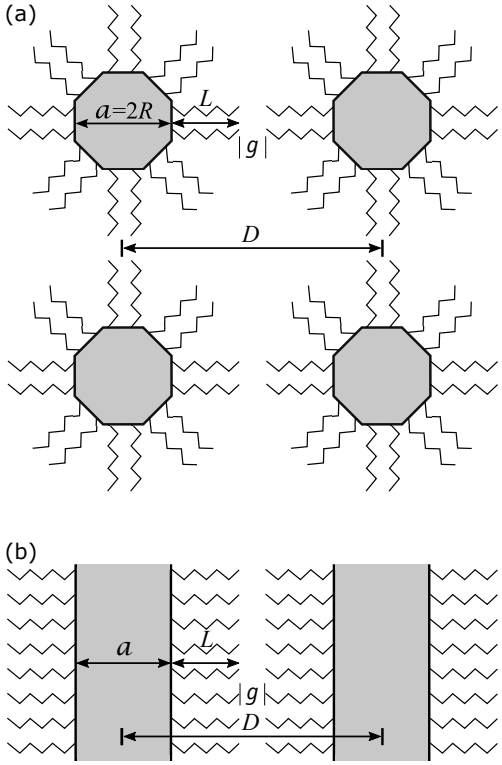

Fig. 1 (a) Three-dimensional cubic lattice of nanocrystals with identical size and shape. The lattice constant D depends on the chemical type and length L of the organic ligands, the ligand-ligand gap g, and the nanocrystal diameter a. (b) Simplified model of the cubic nanocrystal solid. This model represents by design the closest possible contact between opposing ligands is and more amenable to density-functional-theory calculations. It is a periodic array of nanoplatelets, each identical and infinite in two dimensions, with surface orientations and ligand contacts corresponding to the opposing facets of the nanocrystal solid. In this arrangement, the calculated equilibrium value of g is very small, 1-2 Å. Smaller and even negative values are possible for ligands arranged as in panel (a), but steric interactions will ensure the magnitude of g is generally small. This model captures the three main features that control electron transport: quantum size effects in the nanocrystals, the type and size of the ligands as well as the opposing ligand-ligand interactions, and the lattice constant of the nanocrystal solid.

ganization energy[8], Coulomb blockade[14], band offsets due to different nanocrystal or ligand types[15], thermal lattice contraction[16], epitaxially fused nanocrystal solids[17], the space-filling fraction of the nanocrystals[18], etc. This choice allows us to focus on one of the most important aspects of carrier transport: the overlap of quantum-confined wavefunctions on neighboring lattice sites.

The importance of wavefunction overlap for transport is obvious in the case of delocalized "band-like" conduction. There is good evidence for band-like conduction in many nanocrystal solids[19–21] but the generality of this finding is not yet clear[22]. Indeed, mobility data from other nanocrystal solid systems instead show strong evidence of localized "hopping" transport[6,16,23,24]. However, it is important to note that the overlap of wavefunctions controls transport in *both* of these limits. Therefore, our conclusions will likely be valid for a broad range of nanocrystalline solid materials.

1 Approach

The electron and hole wavefunctions in a nanocrystal solid depend on many factors: the electronic properties of the semiconductor; the degree of quantum confinement; the size, type, density, and arrangement of the ligands; and the lattice spacing of the nanocrystals[25,26]. Our strategy is to first use density-functional theory (DFT) in order to capture all of these effects as accurately as possible for a specific nanocrystal solid. We then use the resulting DFT quantum-confined electron and hole states to construct a square-well model whose effective-mass-theory (EMT) wavefunctions reproduce the full DFT wavefunctions as accurately as possible. The overlap integrals of these wavefunctions have a spatial dependence that agrees remarkably well with a broad range of experimental transport data, lending credence to our use of wavefunction overlap as a proxy for transport. Finally, we obtain analytic solutions for the square-well model and use them to predict the behavior of the wavefunction overlap for a broad class of nanocrystal solids. The physically transparent form of these solutions leads to simple principles of carrier transport that are helpful for understanding conductivity in real systems.

The nanocrystal solid of Fig. 1(a), although highly idealized, is still not amenable to accurate DFT calculations for realistically sized nanocrystals. We instead perform the calculations on the closely related system shown in Fig. 1(b). This system consists of parallel nanoplatelets of thickness a, each passivated by ligands of length L and separated by a fixed distance D. These three quantities have close analogs in the three-dimensional nanocrystal solid and so this model can be expected to accurately reflect many of its features, including quantum confinement and ligand-ligand interaction. Of course, certain physical features are missing in the nanoplatelet model, such as the geometrical effects of finite sized nanocrystals; we will analyze these effects using a simple geometrical model. By considering nanoplatelets we necessarily restrict our investigation to a single crystallographic plane with a well-defined ligand coverage, which we assume represents the closest ligand-ligand contact in the full three-dimensional solid of nanocrystals. These assumptions are physically plausible but they also lead to substantial computational simplification: DFT calculations for the nanoplatelet model are far more tractable because the unit cells contain only tens of atoms rather than the hundreds or thousands required for the full solid. This allows us to use the computationally more expensive Heyd-Scuseria-Ernzerhof (HSE) hybrid screened-exchange functional[27], which ensures that electronic properties are represented with excellent accuracy. Details of our computational methods are in the ESI.

2 Results

2.1 Density-functional-theory calculations

We studied one of the most frequently investigated nanoscale materials system: CdSe nanoplatelets passivated by linear chain carboxylate ligands of various lengths[28–32] and, for comparison, a set of short aromatic carboxylate (cinnamate) ligands with various functionalizations[33]. Experimentally, CdSe nanoplatelets are zincblende while CdSe quasi-spherical nanocrystals are wurtzite with different facets. We restrict our attention to the former

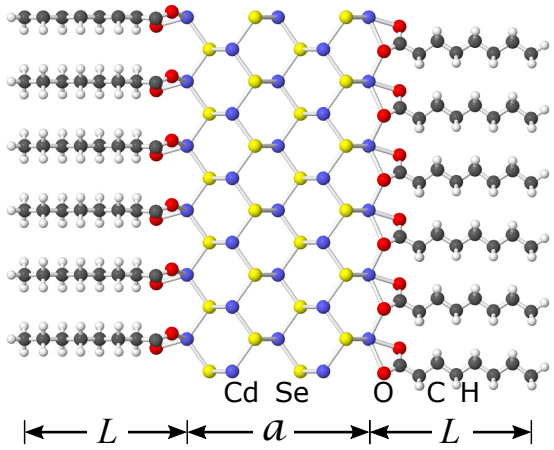

Fig. 2 Structure of an infinite four-monolayer nanoplatelet of CdSe passivated by octanoate ligands, $C_8H_{15}O_2^-$. The relaxed, lowest-energy ligand coordination obtained from DFT total energy calculations is shown, in which the COO^- head groups are coordinated to surface Cd atoms. The labeled quantities correspond to Figs. 1 and 3.

because the chemical coordination of carboxylate ligands to CdSe(001) is well understood: the deprotonated COO^- head group binds at the bridge site between two surface-Cd atoms. (In wurtzite nanocrystals the ligand coordination will be different but the effect on the wavefunction overlap is likely to be minor.) Figure 2 shows the structure obtained from DFT calculations using the Perdew-Burke-Ernzerhof (PBE) exchange-correlation functional[34–36] of a zincblende CdSe nanoplatelet assumed infinite in two dimensions with Cd-terminated (001) facets and passivated by a full monolayer of octanoate ligands. Once the relaxed structure is found it is straightforward to obtain the quantum-confined wavefunctions $\psi(\mathbf{r})$ for the lowest-lying electron and hole states using DFT/HSE. To ensure the accuracy of these wavefunctions we used a plane-wave cutoff energy of 800 eV, twice the default value.

We turn now to our primary quantity of interest, the overlap integral. The full three-dimensional overlap is

$$S_{3d}(D) = \int \psi(\mathbf{r})\psi(\mathbf{r}-\mathbf{D})d^3r, \qquad (1)$$

where $\mathbf{D} = D\hat{\mathbf{x}}$ is the center-to-center separation of the two nanoplatelets. At equilibrium, this separation is determined by the length L of the ligands and their interactions and so it is convenient to write $D = a + 2L + g$, where g is the gap between ligands on adjacent nanoplatelets. Our total-energy calculations show that the optimal g is very small, about 1 to 2 Å for a range of carboxylates. For the rest of this work we set $g = 2$ Å but our conclusions are not sensitive to this choice.

It is straightforward to compute $S_{3d}(D)$ numerically. But it will be more informative to first define a simpler one-dimensional wavefunction $\psi(x)$ by averaging $|\psi(\mathbf{r})|^2$ over y and z and then analyze its overlap,

$$S(D) = \int \psi(x)\psi(x-D)dx. \qquad (2)$$

As an example, the wavefunction $\psi(x)$ for the hole state of the

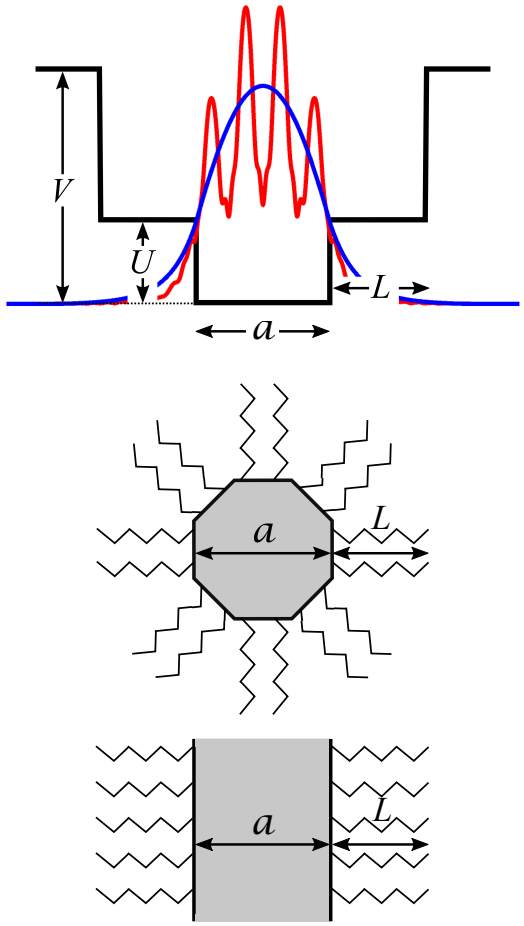

Fig. 3 One-dimensional square-well model of a single nanocrystal or nanoplatelet with organic ligands. The DFT valence wavefunction for a four-monolayer CdSe nanoplatelet (a=12.4 Å) passivated with octanoate ligands (L=11.1 Å), averaged in-plane, is shown in red. The square well that best reproduces the DFT wavefunction has U=1.0 eV and V=4.2 eV and the corresponding effective-mass wavefunction shown in blue. For clarity the square well is not drawn to scale.

4-monolayer (ML) CdSe nanoplatelet with octanoate ligands is shown in Fig. 3 (red curve). The planar averaging obviously affects the value of the overlap but we find this effect to be quite modest, with S typically somewhat larger (approximately by a factor 2-3) than S_{3d} but having a very similar variation with respect to D.

Figure 4 summarizes our numerical results for $S(D)$ using six linear carboxylate ligands of increasing length: the depronated anions of formic, acetic, pentanoic, octanoic, undecylic, and myristic acids. The results are extremely well described by an exponential in the ligand length, $S(L) = S_0 \exp(-L/L_0)$, where the decay length L_0 is 1.42 Å for 4-ML nanoplatelets. To explore the effect of stronger quantum confinement we also calculated the overlaps using 2-ML nanoplatelets. The results are very similar: the prefactor is larger because the wavefunction leakage is greater but the decay length (1.47 Å) is only slightly longer. The results for seven functionalized aromatic ligands are compared in Fig. 6 to the linear ligands. Because of the functionalization, the behavior of the aromatics is more complicated and so we discuss them

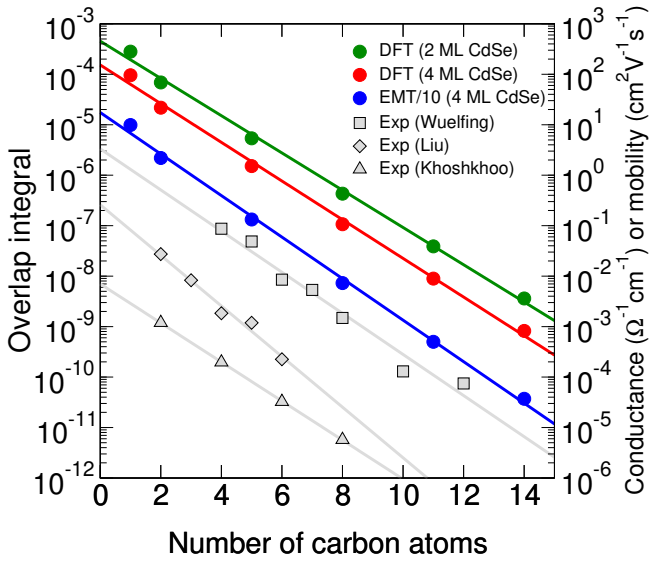

Fig. 4 Theoretical and experimental conductivity in ordered nanocrystal solids. Results from density-functional-theory (DFT) and effective-mass theory (EMT) are in color and show the overlap integrals of the quantum-confined hole-state wave functions for CdSe nanoplatelets as a function of the number of carbon atoms in the ligand molecules. The results for 4-ML platelets obtained from DFT (red) and EMT (blue) are in extremely good agreement; the EMT values are offset by one decade for clarity. The results for 2- and 4-ML nanoplatelets differ by a scale factor but are otherwise very similar despite the very different degree of quantum confinement. The exponential dependence of the DFT overlap integral on ligand length L is characterized by the decay length L_0=1.42 Å for 4-ML platelets. Results from three experiments using similar alkane chain ligands are in gray: conductivity data for Au clusters from Wuelfing *et al.*[37] (squares) yield L_0=1.33±0.06 Å; mobility data for PbSe nanocrystals from Liu *et al.*[23] (diamonds) yield L_0=1.08±0.14 Å; and conductivity data for $Cu_{2-x}Se$ nanocrystals from Khoshkhoo *et al.*[38] (triangles) yield L_0=1.40±0.06 Å.

separately in Section 3.3.

Figure 4 also shows transport data as a function of ligand length from three recent experiments: conductivity data for Au clusters[37], mobility data for PbSe nanocrystals[23], and conductivity data for $Cu_{2-x}Se$ nanocrystals[38]. None of these experiments used CdSe nanocrystals and so the data cannot strictly be compared to our calculations. But all three have in common the use of linear alkane chain ligands (alkanethiols in Ref. 37 and alkanedithiols in Refs. 23 and 38) and therefore, despite having head groups different from carboxylates, their saturated linear carbon chains are otherwise the same. It is striking that the decay lengths for very different nanocrystals are so close (in the range 1.1 to 1.4 Å) and in excellent agreement with our theoretical values. This strongly suggests that the wavefunction overlap is almost entirely determined by the ligands, and that the size, shape, and chemical nature of the nanocrystals play only a minor role. In the following section we introduce an analytical model that explains (1) why the decay length is nearly the same for these different systems; (2) which materials properties determine its value; (3) why it depends only weakly on the nanocrystal size and composition.

2.2 Square-well model and effective-mass theory

To construct a square well representing a single nanoplatelet or nanocrystal, as depicted in Fig. 3, we fix the physical dimensions a and L and then find the potential barriers U and V that lead to the effective-mass wavefunction $\phi(x)$ that best matches $\psi(x)$ in the logarithmic least-squares sense. The resulting $\phi(x)$ for the hole state of the 4-ML CdSe nanoplatelet with octanoate ligands is shown in Fig. 3 (blue curve). See ESI for details of this procedure, including the solution of the stepped square-well problem using a transfer-matrix method, and methods and values for the effective masses of CdSe and the ligands as required in effective-mass theory (EMT).

The EMT overlap integrals $S(D)$ are also plotted in Fig. 4 for 4-ML nanoplatelets. As expected, these values are very close to the DFT values (they are offset for clarity in the plot) and have a very similar decay length of L_0=1.32 Å. This similarity confirms that the square-well model and EMT approach provides an accurate representation of the full DFT overlap integrals. Therefore, we turn next to analyzing the quantities in this model that determine L_0 and from this analysis derive several important characteristics of transport.

3 Discussion

3.1 Wavefunction overlap

The EMT wavefunction $\phi(x)$ is a piecewise function consisting of $\cos(kx)$ in the semiconductor region and predominantly single exponentials $\exp(-\alpha_{\rm lig}|x|)$ and $\exp(-\alpha_{\rm vac}|x|)$ in the ligand and vacuum region, respectively. In the ESI we derive from this wavefunction an expression for the dependence of the overlap integral on L and a:

$$S(D) = \exp(-L/L_0)\xi(a), \tag{3}$$

where $L_0 = 1/2\alpha_{\rm lig}$ and $\xi(a)$ is a decreasing function of nanocrystal size which scales as $1/(a+2L_0)$ for small a and is independent of L. This expression leads to two important conclusions. (1) The exponential decay length L_0 has no explicit dependence on a and hence is primarily an intrinsic property of the ligands. This explains why experiments involving alkane chain ligands exhibit very similar decay lengths even though the nanocrystals themselves are of different sizes and even different materials. (2) For fixed ligand length L, the overlap integral decreases with the size a because of reduced wavefunction leakage. This is in agreement with our DFT results for the overlap values of 2- and 4-ML nanoplatelets (Fig. 4).

3.2 Behavior of the decay length

We turn now to finding an explicit expression for the decay length L_0 by determining the exponent $\alpha_{\rm lig} = [2m_{\rm lig}(U-E)]^{1/2}/\hbar$, where $m_{\rm lig}$ is the effective mass in the ligand region and E is the energy of the lowest-lying bound state. Exact values for E can only be found numerically or graphically, but by linearizing the square-well equation (see ESI) we obtain a compact analytic expression for the decay length,

$$L_0 = \mathscr{L}_0\left[1 - \frac{2}{1+(U/U_0)^{1/2}}\right]^{-1/2}, \tag{4}$$

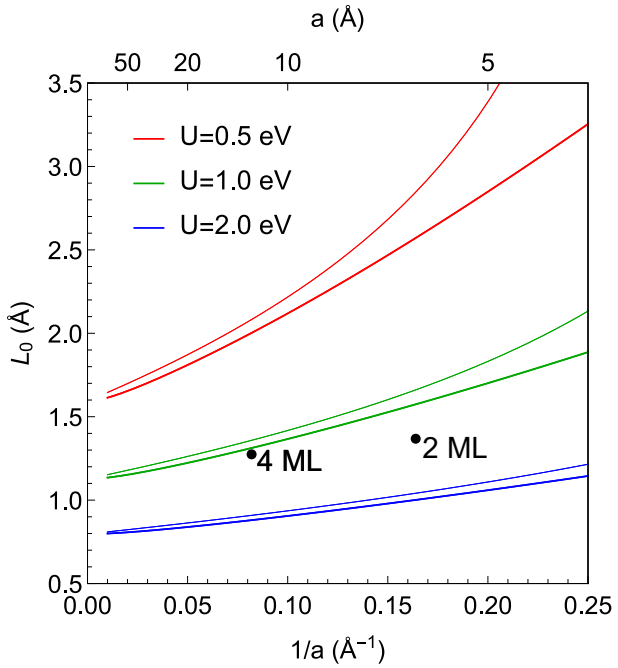

Fig. 5 Decay length L_0 obtained from effective-mass theory as a function of platelet thickness (or nanocrystal diameter) a and square-well barrier height U. Thick lines show exact results. Thin lines show the linear-order decay length of Eq. (4). The linear-order values for 2- and 4-ML CdSe nanoplatelets are marked by black circles and agree well with the decay lengths obtained by numerically fitting the full DFT results in Fig. 4.

where

$$\mathscr{L}_0 = \frac{1}{2}\frac{\hbar}{(2m_{\rm lig}U)^{1/2}} \tag{5}$$

is the decay length in the limit of large U and a and we have defined a characteristic energy scale,

$$U_0 = \frac{\hbar^2}{2m_{\rm lig}a^2}, \tag{6}$$

which also sets a lower limit of validity for the barrier U. For carboxylates, U is of order 1 eV while U_0 is much smaller (less than 0.1 eV for 2-ML nanoplatelets). In this regime it is easy to see that L_0 scales as $U^{-1/2}$ to lowest order. The linearization also sets a lower limit of validity for the size, $a_{\rm min} = 2\mathscr{L}_0$, which is of order 2 Å. This criterion is easily satisfied for most nanoplatelets and nanocrystals of practical interest. In this regime it is easy to show that L_0 is equal to the size-independent value $\mathscr{L}_0$ multiplied to lowest order by $1+a_{\rm min}/a$. The smallness of the size-dependent correction term explains the insensitivity of L_0 to the nanoplatelet size a found in our DFT results for 2- and 4-ML nanoplatelets.

Figure 5 illustrates these two trends numerically. The barrier heights U provided by carboxylate ligands are in the range 1 to 2 eV (between the green and blue curves) and thus the decay length L_0 is in the range 1.0 to 1.5 Å. In this regime L_0 is only very weakly dependent on the nanocrystal size and is essentially independent of its electronic properties such as band gap and effective mass. This explains why the experimental transport data in Fig. 4—from solids of Au, PbSe, and $Cu_{2-x}Se$ nanocrystals but with chemically similar alkane chain ligands—all have very similar values of L_0.

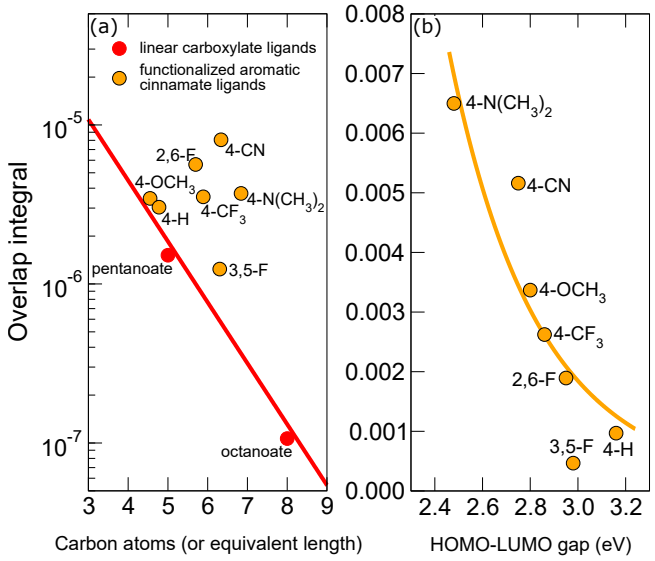

Fig. 6 (a) DFT overlap integrals of the quantum-confined hole-state wave functions for 4-ML CdSe nanoplatelets, comparing linear and functionalized aromatic ligands. For the aromatic ligands, the length of the ligand (projected onto the CdSe surface normal) was used to define the equivalent number of carbon atoms for a linear chain. (b) DFT overlap integrals rescaled by by $1/\exp(-L/L_0)$, as a function of the HOMO-LUMO gap E_g calculated within DFT/PBE. The curve is a fit to $\exp(-\beta E_g^{1/2})$, which is the expected behavior for wavefunction confined by a square-well with barrier height E_g.

3.3 Functionalized aromatic carboxylate ligands

We turn now to a chemically more complex set of ligands: the conjugate bases of seven functionalized cinnamic acid molecules recently investigated in Ref. 33. These ligands have carboxylate head groups and are therefore very likely to coordinate to CdSe(001) in the same way as the linear carboxylates, making them especially suitable for direct comparison. But their additional functional groups—of nitrogen, fluorine, oxygen, and methyl groups—make their role in wavefunction overlap more complicated. Nevertheless, we show here that their predicted behavior can be qualitatively and even quantitatively understood using the same approach developed above for the linear ligands.

The seven ligands we investigated are cinnamate (4-H), 4-cyanocinnamate (4-CN), 4-dimethylaminocinnamate (4-$N(CH_3)_2$), 3,5-difluorocinnamate (3,5-F), 2,6-difluorocinnamate (2,6-F), 4-trifluoromethylcinnamate (4-CF_3), and methoxycinnamate (4-OCH_3). Following the same procedure as for the linear ligands, we computed the DFT overlap integrals for hole-state wavefunctions of 4-ML CdSe nanoplatelets passivated by cinnamate ligands. The results are compared in Fig. 6(a) to the linear carboxylate results of Fig. 4. The cinnamate ligands are similar in length to pentanoate and so it is not surprising that their overlaps are of the same order as for that ligand, albeit considerably larger. However, there is no discernible trend among the overlaps with respect to the cinnamate length.

All of these findings can be understood by analyzing the electronic structure of the cinnamates, specifically their HOMO-LUMO gaps E_g. For the linear ligands, E_g is a slowly varying function of length L. But for the cinnamates, the different func-

tionalizations lead to very different values of E_g even for ligands of similar length. We used DFT/PBE to estimate E_g of isolated cinnamic acid ligands and found them to have much smaller values (in the range 2.5 to 3.2 eV) than pentanoic acid (5.3 eV). Smaller gaps imply lower barrier energies U and therefore greater wavefunction leakage and larger wavefunction overlaps, which is consistent with the results in Fig. 6(a).

This interpretation can be confirmed quantitatively by disentangling the effects of the two major factors controlling the overlap, the ligand length L and the HOMO-LUMO gap E_g. In Fig. 6(b) we have removed the effect of varying lengths by dividing the cinnamate overlaps by $\exp(-L/L_0)$, where the decay length L_0 is 1.42 Å for these 4-ML nanoplatelets. This reveals the very simple, physically transparent dependence of the scaled overlap on the HOMO-LUMO gap. According to Eq. (5) this dependence is exponential in the square root of E_g, which is quantitatively consistent with the results in Fig. 6(b).

Finally, we note that the different cinnamate functionalizations also lead to widely varying electric dipole moments (from -2.9 to $+6.8$ D for the free cinnamic acid molecules, as reported in Ref. 33). These dipole moments are correlated with the HOMO-LUMO gaps and hence their role in the wavefunction overlap cannot be independently analyzed. Moreover, when bound to the nanocrystal surface, these molecular dipole moments are strongly compensated by an interface dipole[39].This compensation makes the intrinsic molecular dipole a less useful quantity than the HOMO-LUMO gap for analyzing wavefunction overlap.

3.4 Geometrical effect of nanocrystal size

The results obtained so far have assumed a planar geometry with a single gap g between opposing ligands. For nanoplatelets this is a reasonable assumption and so no further issues arise. But for finite nanocrystals we must address the geometrical effect of curvature on the overlap of wavefunctions.

The decay of a wavefunction from the surface of a sphere with radius R into the vacuum can be accurately modeled by the function $f_R(\mathbf{r}) = \exp(-r/L_1)$ for $r > R$ (outside the sphere) and unity inside. According to our DFT calculations the decay length L_1 is of order 1 Å. Consider now the integral $F(R) = \int f_R(\mathbf{r}) f_R(\mathbf{r}-\mathbf{D}) d^3r$ where, for simplicity, we set the center-to-center separation D such that the spheres are just touching.

In the ESI we show that for sphere sizes satisfying $R > L_1$ this integral scales linearly with the sphere size, $F(R) \propto RL_1^2$. This additional scaling with the sphere size modifies the planar expression for $S(D)$, as we summarize next.

3.5 Overall behavior of wavefunction overlap.

The effect of finite curvature of the nanocrystals, which reduces overlap for small sizes, is counteracted by the effect of wavefunction leakage, which increases overlap for small sizes. This can be seen by combining the expressions obtained above to express the overall behavior of the wavefunction overlap:

$$S(D) \propto \left(\frac{a+2L}{a+2L_0}\right) L_1^2 \exp(-L/L_0). \quad (7)$$

Here, $a+2L$ is the effective size of the spherical nanocrystal including its ligand shell. For very short ligands or large nanocrystals the term in parentheses approaches unity, indicating that nanocrystal size plays only a minor role in electron transport. Experimental investigation of this predicted behavior has, to our knowledge, not yet been undertaken.

4 Relation to experiments

It has long been recognized experimentally that shorter ligands are a promising route to better conductivity[3,4,7]. This strategy can be implemented using ligand exchange after the nanocrystal growth has completed, so that the colloidal synthesis itself does not need to be changed. For example, inorganic molecular metal chalcogenide ligands such as Sn_2S_6 increase the conductivity of CdSe nanocrystal films by orders of magnitude compared to as-grown films with organic ligands[40,41]. The ultimate limit of these inorganic metal ligands is a single monolayer of passivating atoms. Ligand exchange to create such a layer of passivating chlorine atoms has been demonstrated to greatly increase the conductivity of Au nanoparticles[42]. Although we did not address inorganic ligands in our investigation, our model could be readily generalized to include them as well.

Some of these ligand exchange methods employ hydrazine, N_2H_6, as part of the post-growth processing[40]. Hydrazine treatment by itself was also shown to greatly increase the conductivity of PbSe nanocrystal solids and even to enable reversible switching of the conduction between n-type and p-type, suggesting that hydrazine dopes the material by surface charge transfer[43]. Subsequent theoretical studies of hydrazine adsorption on PbSe indicated the material actually remains intrinsic but other possibilities—such as dissociative adsorption to form NH_2 (which was predicted to dope PbSe) or etching of the surface to create vacancy defects—remain relatively unexplored[44]. At any rate, these doping strategies, while interesting and potentially useful, are outside the scope of our overlap model.

Another approach to increasing conductivity in nanocrystal solids is by photoexcitation. In this approach, an electron-hole pair created by an incident photon decays nonradiatively via Auger recombination. The resulting energy excites the electron above its ionization threshold and creates a quasi-free carrier. This strategy can lead to photoconductivity in nanocrystal solids exceeding the dark conductivity by 2-3 orders of magnitude even at relatively weak light excitation[41,45]. This enhancement of the photocurrent, which is due to high mobility of the photoexcited states, arises in disordered semiconductors from variable-range hopping. However, at room temperature, direct hopping between neighboring nanocrystals becomes dominant and therefore the photocurrent becomes proportional to the overlap integral[9]. The nature and magnitude of the disorder only affect the non-exponential prefactor of the current. Hence, ligands control the photoconductivity at room temperature as well as the dark current.

5 Conclusions

Our main finding—obtained by combining first-principles numerical calculations and analytic approaches—is that electron trans-

port in nanocrystal solids is controlled primarily by the ligand molecules. In particular, the overlap of wavefunctions on neighboring nanocrystals decays exponentially with the ligand length and the characteristic decay length scales with the square root of the potential barrier provided by the ligand shell, with a weak linear dependence on the inverse size of the nanocrystals. For saturated hydrocarbon chains this decay length has the predicted value 1.4 Å with small variations of order 0.1 Å depending on the size and type of the nanocrystal. Because the decay length is determined by the barrier height provided by the ligands, it can be controlled using chemistry through the choice of ligand or using geometry through the concentration of ligand molecules. These findings may enable the rational design of new materials having specific transport properties.

Conflicts of interest

There are no conflicts to declare.

Acknowledgements

This work was supported by the Office of Naval Research through Award N0001418WX01839 and through the Naval Research Laboratory's Basic Research Program. A.R.K. acknowledges support from a National Research Council fellowship at the Naval Research Laboratory. Computations were performed at the DoD Major Shared Resource Center at AFRL.

Notes and references

1 C. B. Murray, C. R. Kagan and M. G. Bawendi, *Science*, 1995, **270**, 1335–1338.
2 M. V. Kovalenko, L. Manna, A. Cabot, Z. Hens, D. V. Talapin, C. R. Kagan, V. I. Klimov, A. L. Rogach, P. Reiss, D. J. Milliron, P. Guyot-Sionnnest, G. Konstantatos, W. J. Parak, T. Hyeon, B. A. Korgel, C. B. Murray and W. Heiss, *ACS Nano*, 2015, **9**, 1012–1057.
3 C. R. Kagan, E. Lifshitz, E. H. Sargent and D. V. Talapin, *Science*, 2016, **353**, 885.
4 C. R. Kagan, *Chemical Society Reviews*, 2019, **48**, 1626–1641.
5 J. H. Choi, A. T. Fafarman, S. J. Oh, D. K. Ko, D. K. Kim, B. T. Diroll, S. Muramoto, J. G. Gillen, C. B. Murray and C. R. Kagan, *Nano Letters*, 2012, **12**, 2631–2638.
6 P. Guyot-Sionnest, *Journal of Physical Chemistry Letters*, 2012, **3**, 1169–1175.
7 C. R. Kagan and C. B. Murray, *Nature Nanotechnology*, 2015, **10**, 1013–1026.
8 N. Yazdani, S. Andermatt, M. Yarema, V. Farto, M. H. Bani-Hashemian, S. Volk, W. M. Lin, O. Yarema, M. Luisier and V. Wood, *Nature Communications*, 2020, **11**, 2852.
9 A. Shabaev, Al. L. Efros and A. L. Efros, *Nano Letters*, 2013, **13**, 5454–5461.
10 S. Toso, D. Baranov, D. Altamura, F. Scattarella, J. Dahl, X. Wang, S. Marras, A. P. Alivisatos, A. Singer, C. Giannini and L. Manna, *ChemRxiv (preprint)*, 2020.
11 J. Yang and F. W. Wise, *Journal of Physical Chemistry C*, 2015, **119**, 3338–3347.
12 D. Bozyigit, W. M. Lin, N. Yazdani, O. Yarema and V. Wood, *Nature Communications*, 2015, **6**, 6180.
13 Y. Wei, M. V. Tokina, A. V. Benderskii, Z. Zhou, R. Long and O. V. Prezhdo, *The Journal of Chemical Physics*, 2020, **153**, 044706.
14 H. E. Romero and M. Drndic, *Physical Review Letters*, 2005, **156801**, 1–4.
15 Q. Zhou, Y. Cho, S. Yang, E. A. Weiss, T. C. Berkelbach and P. Darancet, *Nano Letters*, 2019, **19**, 7124–7129.
16 R. H. Gilmore, S. W. Winslow, E. M. Lee, M. N. Ashner, K. G. Yager, A. P. Willard and W. A. Tisdale, *ACS Nano*, 2018, **12**, 7741–7749.
17 A. Abelson, C. Qian, T. Salk, Z. Luan, K. Fu, J. G. Zheng, J. L. Wardini and M. Law, *Nature Materials*, 2020, **19**, 49–55.
18 X. Zha and A. Travesset, *Journal of Chemical Physics*, 2020, **152**, 1–8.
19 E. Talgorn, Y. Gao, M. Aerts, L. T. Kunneman, J. M. Schins, T. J. Savenije, M. A. Van Huis, H. S. Van Der Zant, A. J. Houtepen and L. D. Siebbeles, *Nature Nanotechnology*, 2011, **6**, 733–739.
20 Y. Liu, N. Peard and J. C. Grossman, *Journal of Physical Chemistry Letters*, 2019, **10**, 3756–3762.
21 X. Lan, M. Chen, M. H. Hudson, V. Kamysbayev, Y. Wang, P. Guyot-Sionnest and D. V. Talapin, *Nature Materials*, 2020, **19**, 323–330.
22 H. Oberhofer, K. Reuter and J. Blumberger, *Chemical Reviews*, 2017, **117**, 10319–10357.
23 Y. Liu, M. Gibbs, J. Puthussery, S. Gaik, R. Ihly, H. W. Hillhouse and M. Law, *Nano Letters*, 2010, **10**, 1960–1969.
24 K. Whitham, J. Yang, B. H. Savitzky, L. F. Kourkoutis, F. Wise and T. Hanrath, *Nature Materials*, 2016, **15**, 557–563.
25 O. L. Lazarenkova and A. A. Balandin, *Journal of Applied Physics*, 2001, **89**, 5509–5515.
26 F. M. Gómez-Campos, S. Rodríguez-Bolívar and M. Califano, *ACS Photonics*, 2016, **3**, 2059–2067.
27 J. Heyd, G. E. Scuseria and M. Ernzerhof, *The Journal of Chemical Physics*, 2003, **118**, 8207–8215.
28 S. Ithurria, M. D. Tessier, B. Mahler, R. P. Lobo, B. Dubertret and A. L. Efros, *Nature Materials*, 2011, **10**, 936–941.
29 B. Mahler, B. Nadal, C. Bouet, G. Patriarche and B. Dubertret, *Journal of the American Chemical Society*, 2012, **134**, 18591–18598.
30 A. Riedinger, F. D. Ott, A. Mule, S. Mazzotti, P. N. Knüsel, S. J. Kress, F. Prins, S. C. Erwin and D. J. Norris, *Nature Materials*, 2017, **16**, 743–748.
31 T. Galle, M. Kazes, R. Hübner, J. Lox, M. Samadi Khoshkhoo, L. Sonntag, R. Tietze, V. Sayevich, D. Oron, A. Koitzsch, V. Lesnyak and A. Eychmüller, *Chemistry of Materials*, 2019, **31**, 5065–5074.
32 C. Meerbach, C. Wu, S. C. Erwin, Z. Dang, A. Prudnikau and V. Lesnyak, *Chemistry of Materials*, 2020, **32**, 566–574.
33 D. M. Kroupa, M. Vörös, N. P. Brawand, B. W. McNichols, E. M. Miller, J. Gu, A. J. Nozik, A. Sellinger, G. Galli and M. C. Beard, *Nature Communications*, 2017, **8**, 15257.
34 G. Kresse and J. Furthmüller, *Physical Review B*, 1996, **6**, 15–50.
35 P. E. Blöchl, *Physical Review B*, 1994, **50**, 17953–17979.
36 J. P. Perdew, K. Burke and M. Ernzerhof, *Physical Review Letters*, 1996, **77**, 3865–3868.
37 W. P. Wuelfing, S. J. Green, J. J. Pietron, D. E. Cliffel and R. W. Murray, *Journal of the American Chemical Society*, 2000, **122**, 11465–11472.
38 M. S. Khoshkhoo, J. F. L. Lox, A. Koitzsch, H. Lesny, Y. Joseph, V. Lesnyak and A. Eychmüller, *ACS Applied Electronic Materials*, 2019, **1**, 1560–1569.
39 P. R. Brown, D. Kim, R. R. Lunt, N. Zhao, M. G. Bawendi, J. C. Grossman and V. Bulović, *ACS Nano*, 2014, **8**, 5863–5872.
40 M. V. Kovalenko, M. Scheele and D. V. Talapin, *Science*, 2009, 1417–1420.
41 J. Lee, M. V. Kovalenko, J. Huang, D. S. Chung and D. V. Talapin, *Nature Nanotechnology*, 2011, **6**, 348–352.
42 M. Zanella, L. Maserati, M. P. Leal, M. Prato, R. Lavieville, M. Povia, R. Krahne and L. Manna, *Chemistry of Materials*, 2013, **25**, 1423–1429.
43 D. V. Talapin and C. B. Murray, 2005, **9593**, 86–89.
44 A. Kutana and S. C. Erwin, *Physical Review B*, 2011, **235419**, 1–4.
45 P. Nagpal and V. I. Klimov, *Nature Communications*, 2011, **2**, 486.

TOC graphics: Theoretical modeling of wavefunction overlap in nanocrystal solids elucidates the important role played by ligands in electron transport